CHAPTER

19

$^{40}Ar/^{39}Ar$ constraints on the tectonic evolution of the late Paleozoic and early Mesozoic accretionary complex of coastal central Chile

Laura E. Webb, Keith A. Klepeis

Department of Geology, University of Vermont, Burlington, VT, United States

1 Introduction

The Coast Ranges of north-central Chile record a long history (>300 Myr) of convergent margin tectonism since the Carboniferous, including multiple phases of arc magmatism, shortening, extension, and margin-parallel shear. Basement rocks preserve gradients in age, strain, and depth of exposure from south to north along the margin. The latitude of 34°S has long been considered to mark a transition from a well-preserved late Paleozoic-early Mesozoic accretionary complex to the south (Fig. 1A) (Willner et al., 2009) to a margin modified by subduction erosion to the north (e.g., Kay et al., 2005). While the metamorphic and structural evolution of the accretionary complex has been examined in detail south of ~34–37°S (Willner, 2005; Willner et al., 2005, 2009; Richter et al., 2007), and the Paleozoic-Mesozoic history of magmatism from ~31°S to 37°S is established (e.g., Parada et al., 1999; Vásquez et al., 2011), much less is known about the structural evolution of the Coast Ranges just north of 34°S. This section of coastline preserves superb exposures of igneous and metamorphic rocks that facilitate combined structural and $^{40}Ar/^{39}Ar$ geochronologic analyses across strain gradients to reveal multiple tectonic reactivations within a long-lived plate boundary zone.

Many previous studies have noted the significance of ~NW-striking structures in central Chile. Creixell et al. (2011) concluded that Late Jurassic deformation and magmatism between 33° and 33°45′S was strongly controlled by NW-WNW-striking fractures and that these lineaments, inferred to exert a control as basin-bounding faults in the Cenozoic (e.g., Rivera and Cembrano, 2000), date to at least that time. Additionally, recent studies of the great 2010 Maule earthquake (e.g., Arriagada et al., 2011; Aron et al., 2013) highlight the importance of the reactivation of NW-trending structures in the middle crust during coseismic deformation in the upper plate of the Chile subduction zone. Near Pichilemu, intraplate deformation above the Andean subduction zone at depths ranging from 12 to 20 km below the surface nucleated on steep (≥75°), NW-striking (320°) structures that formed during previous periods of tectonic activity. Approximately 100 km to the north near Valparaíso, where approximately seven large to great historical earthquakes have been recorded (Beck et al., 1998), studies of active faulting determined that the deep-seated NW-striking structures pose the greatest seismic hazard (Sabaj, 2008).

Andean Tectonics. https://doi.org/10.1016/B978-0-12-816009-1.00020-4

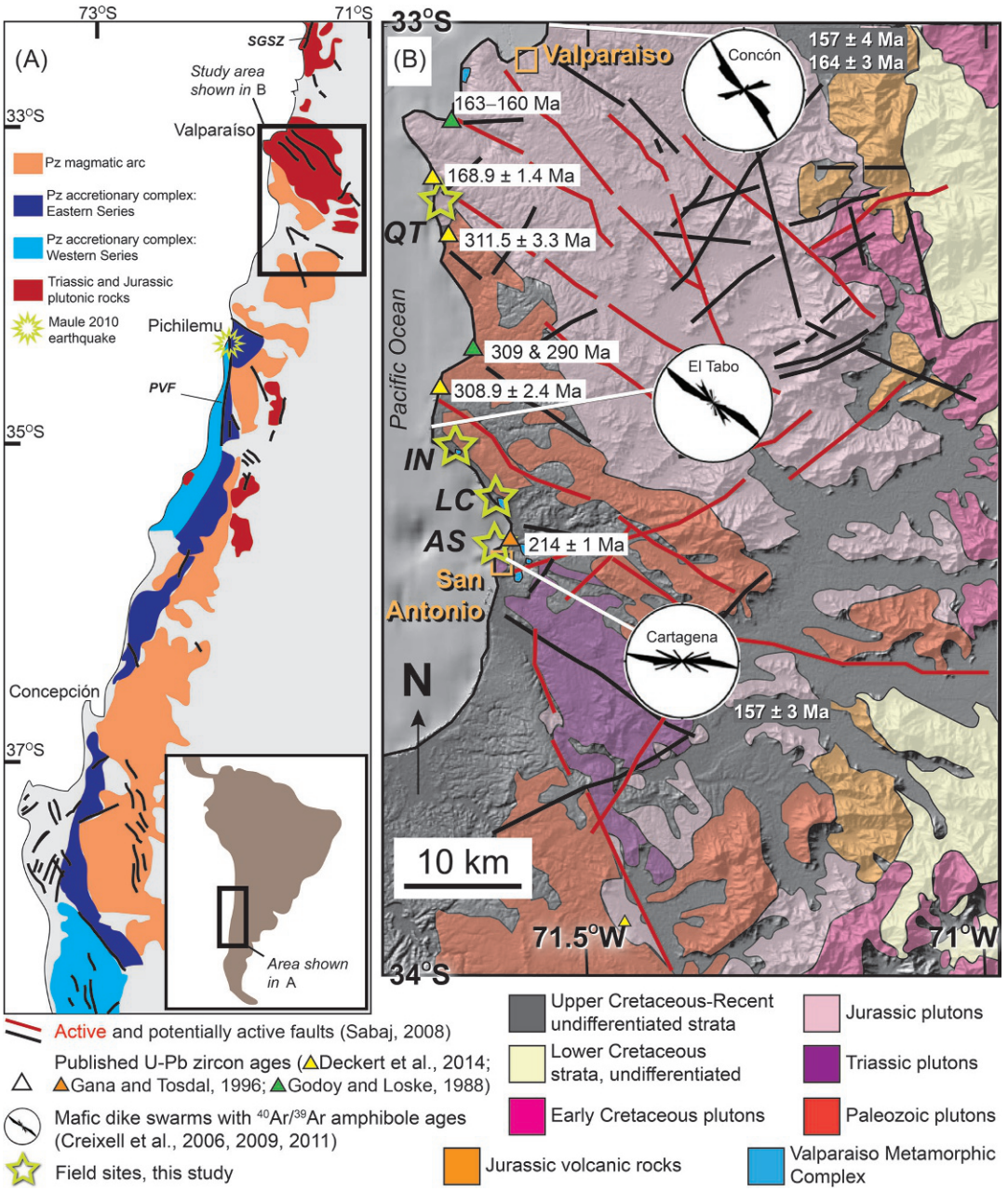

FIG. 1

Tectonic and geologic maps of the study area. (A) Map of the coastal Andes in central Chile showing the Paleozoic-Mesozoic accretionary complex, magmatic belts, and major fault systems (modified after Deckart et al., 2014). Box-labeled study area indicates region shown in (B). Abbreviations for faults and shear zone discusses in text: PVF = Pichilemu-Vichuquén Fault; SGSZ = Silla del Gobernador Shear Zone. (B) Geologic map of the study area compiled from Parada et al. (2005), Creixell et al. (2006), Gana and Tosdal (1996), and Sabaj (2008); DEM background was constructed using GeoMapApp software and sources. Studied sites are abbreviated on map as follows: QT = Quintay; IN = Isla Negra; LC = Las Cruces; AS = Agua Salada.

The data presented in this manuscript provide evidence that the ~NW-striking structural grain formed as early as the Late Carboniferous and support the notion that the strike of active faults (Fig. 1B) mimics basement structural trends that formed and were exploited multiple times along this long-lived convergent margin. The results of this study are thus pertinent to an understanding of seismic hazards within the Andean margin because the rheology of the crust is deeply influenced by its kinematic and thermal history (Handy et al., 2007).

1.1 Geologic background

The Coast Ranges of north-central Chile (Fig. 1) record the initiation of subduction beneath the margin of Gondwana during Late Carboniferous times (Forsythe, 1982). As subduction began, an accretionary complex developed that has long been recognized as a paired metamorphic belt (Aguirre et al., 1972; Hervé, 1988) in the sense of Miyashiro (1961). A high-P/low-T Western Series is composed of continental rocks and accreted oceanic lithologies; the low-P/high-T Eastern Series is composed mainly of metagraywacke and metapelite of turbidite origin (Hervé, 1977; Willner et al., 2005). Metamorphic conditions in the Western Series reached pressures of 7–11 kbar and temperatures of 380–420°C during the 305–290 Ma interval (Willner, 2005; Willner et al., 2005). In the Eastern Series, metamorphic mineral assemblages mostly reflect contact metamorphism related to the shallow (~3 kbar) emplacement of 296–301 Ma plutons that form part of a Late Carboniferous-Early Permian magmatic arc (Parada et al., 1999; Willner, 2005). The Eastern Series also records an initial period of frontal accretion within the margin that shifted to basal accretion in the Western Series after ~300 Ma as late Paleozoic magmatism began (Richter et al., 2007). The principal evolution of this accretionary system appears to have ended by ~225 Ma when a major tectonic change from a convergent to an extensional/strike-slip regime occurred (Willner et al., 2009).

Whereas the architecture of the late Paleozoic accretionary complex of the Andean margin is well preserved between latitudes 36°S and 35°S, sections exposed north of 35°S become increasingly affected by younger tectonic events. Between 34°S and 35°S, two main episodes of post-accretionary deformation altered the complex (Willner et al., 2009). The first occurred in the Jurassic when foliations were steepened and mineral lineations were rotated into N-S orientations during left-lateral strike-slip activity. This latter period culminated in the formation of tight, upright folds and steep cataclastic shear zones. A second episode of cataclastic deformation occurred at ~100 Ma simultaneously with the closure of extensional basins and uplift of the forearc. This latter period was characterized by transpressional deformation and left-lateral motion on margin-parallel structures, including the Pichilemu-Vichuquén Fault (PVF, Fig. 1).

Between 34°S and 33°S latitude, the coastal ranges are composed mainly of upper Paleozoic to Lower Cretaceous intrusive and volcanic rock (Hervé et al., 1988; Gana et al., 1996; Gana and Tosdal, 1996; Wall et al., 1996). The oldest and dominant belt at these latitudes is the Santo Domingo Complex, which includes Late Carboniferous-Early Permian hornblende and biotite-bearing tonalite with abundant enclaves, granodiorite, and minor granite (Siña and Parada, 1985; Siña, 1987a,b; Wall et al., 1996; Parada et al., 1999). An intrusive contact between rocks of the Santo Domingo Complex and a small exposure of gneiss inferred to be a part of the late Paleozoic Western Series is exposed about 20 km south of the city of Valparaíso near Isla Negra and Las Cruces (Webber et al., 2015) (Fig. 1B). Godoy and Loske (1988) obtained two zircon U-Pb ages of ~309 and ~290 Ma from orthogneiss near this site, and Deckart et al. (2014) also reported a ~309 Ma U-Pb zircon age from a nearby locality. These ages are similar to those obtained by Berg and Charrier (1987) and Hervé et al. (1988) from the Santo Domingo Complex. Nevertheless, the age of metamorphism and deformation in these

rocks is only poorly known (Creixell et al., 2011 and references therein). In this chapter, we refer to the exposures of deformed and metamorphosed rock between Isla Negra and San Antonio (Fig. 1B) as the Valparaíso Metamorphic Complex. North of 33° S, Mesozoic plutonic rocks dominate the geology of the coastal ranges.

East of the Santo Domingo Complex, Vásquez et al. (2011) identified three pulses of Triassic-Jurassic magmatism that young to the east and show a progression toward more mafic compositions with time. The first pulse, at 225–220 Ma, produced granitic rocks that record mainly crustal sources, although some mantle contributions are recognizable. A second pulse of bimodal magmatism at 210–197 Ma was accompanied by crustal extension and shows higher proportions of mantle-derived melts. An Early Jurassic suite, referred to as the Limarí Complex, includes leucogranite, granite porphyries, and mantle-derived gabbro (Parada et al., 1999). In contrast, the Middle to Late Jurassic Papudo-Quintero Complex records more juvenile components in a suite of enclave-rich hornblende-bearing tonalite, hornblende-pyroxene diorite, and biotite granite. This latter complex overlaps temporally with syntectonic mafic dike swarms that occur between San Antonio and Valparaíso (Fig. 1B) (Creixell et al., 2006, 2009, 2011). All of these episodes display geochemical signatures characteristic of subduction-related magmatism.

The emplacement of the various suites of plutonic and volcanic rocks into the Andean margin during the Triassic and Jurassic was accompanied by widespread extension and transtension in northern Argentina and Chile (Mpodozis and Ramos, 2008). By the end of the Triassic, continental-scale extension and rifting was at its peak. In the Early Jurassic, a series of spreading centers formed between North and South America, marking the beginning of Pangea break-up (Mpodozis and Ramos, 2008). Motion along these spreading centers produced a component of oblique subduction along the western margin of South America. Eventually subduction led to the formation of a new magmatic arc from southern Peru to central Chile. East of the study area, this period of magmatism formed the Illapel Plutonic Complex, which consists of hornblende bearing tonalite, trondhjemite, and granodiorite (Morata et al., 2009), and volcanic sequences associated with extension (Morata and Aguirre, 2003). Jurassic-Early Cretaceous convergence or oblique convergence also produced a series of extensional and transtensional faults and basins from northern Chile to Patagonia (Dalziel, 1981; Mpodozis and Ramos, 1989; Ramos and Folguera, 2005; Cembrano et al., 2005). Many of these basins were inverted during mid-Cretaceous compression, which resulted in the uplift, crustal shortening, and the formation of steep dextral and dextral-reverse shear zones in north-central Chile (Arancibia, 2004).

2 Methods

Geologic field work included the mapping, measurement, and documentation of structural elements and their relative timing with respect to each other, igneous intrusion, and metamorphism. Samples were selected for $^{40}Ar/^{39}Ar$ geochronology after petrographic and microstructural analyses. Microstructural analyses (Vernon, 2004; Passchier and Trouw, 2005) were conducted on oriented thin sections to evaluate the relative timing of metamorphism and deformation, evidence of the former presence of melt, deformation mechanisms operative at various stages in a variety of minerals (e.g., as a function of temperature of deformation), kinematics and strain gradients, evidence for recovery and static recrystallization (e.g., grain boundary area reduction/polygonal textures), and brittle overprints, etc.

$^{40}Ar/^{39}Ar$ analyses were performed at the University of Vermont Noble Gas Geochronology Laboratory. Inclusion-free mineral grains were handpicked from crushed rock samples under a bioptic microscope after having been washed, sonified, and dried to remove any adhering particulate matter. Grains from each sample were loaded into aluminum foil packets, arranged in a suprasil vial, and placed in an aluminum canister for irradiation. Samples were irradiated with multigrain aliquots of Fish Canyon Tuff Sanidine to act as a flux monitor (28.03 Ma; Renne et al., 1998) to monitor the neutron dose, and Ca and K salts were also irradiated to determine corrections for interfering nuclear reactions. Samples were irradiated for eight hours at the Cadmium-Lined In-Core Irradiation Tube (CLICIT) reactor of Oregon State University, Corvallis, Oregon, USA.

Laser step heating for $^{40}Ar/^{39}Ar$ dating was conducted with a Santa Cruz Laser Microfurnace 75-W diode laser system. With the exception of muscovite and flux monitors, samples were loaded directly into wells in a copper sample holder. Muscovite and sanidine grains were loaded into degassed Nb foil packets before being loaded in the wells in the sample holder. The gas released during heating was purified with SAES getters and argon isotopes were analyzed on a Nu Instruments Noblesse magnetic sector noble gas mass spectrometer in peak-hopping mode during step-heating analyses. Data from samples and flux monitors were corrected for blanks, mass discrimination, atmospheric argon, neutron-induced interfering isotopes, and the decay of ^{37}Ar and ^{39}Ar. Mass discrimination was calculated by analyzing known aliquots of atmospheric argon for which the measured $^{40}Ar/^{36}Ar$ was compared with an assumed atmospheric value of 298.56 (Lee et al., 2006). Correction factors used to account for interfering nuclear reactions for the irradiated samples are: $(^{40}Ar/^{39}Ar)_K = 3.48\times10^{-3} \pm 1.66\times10^{-3}$, $(^{36}Ar/^{37}Ar)_{Ca} = 2.3\times10^{-4} \pm 0.6\times10^{-4}$, $(^{39}Ar/^{37}Ar)_{Ca} = 6.6\times10^{-4} \pm 0.6\times10^{-4}$. A linear interpolation was used to calculate J factors for samples based on sample position between flux monitor packets in the irradiation tube.

Age calculations were achieved using both an in-house data reduction program and Isoplot 3.0 (Ludwig, 2003). Weighted mean ages are reported, and plateau ages are reported if sufficient criteria were met (see McDougall and Harrison, 1999). Errors on plateaus and weighted mean ages are quoted at the 1σ level and include precision associated with measurement of the irradiation parameter, J, for flux monitors. A summary data table with geographic coordinates for samples as well as the full data tables for all $^{40}Ar/^{39}Ar$ analyses are provided in Appendix 1 in the online version at https://doi.org/10.1016/B978-0-12-816009-1.00020-4 and Appendix 2 in the online version at https://doi.org/10.1016/B978-0-12-816009-1.00020-4, respectively.

3 Results

3.1 Isla Negra

3.1.1 Field relationships

The coastal outcrops near Isla Negra (Figs. 1B and 2A) expose two intrusive suites of the Santo Domingo Complex: the Punta de Tralca and the Estero Córdoba units (Parada et al., 1999). The former is a layered intrusion of mostly tonalitic to granodioritic composition that hosts numerous (up to 50% by volume) fine-grained, mafic enclaves. The Estero Córdoba unit is mainly composed of massive enclave-poor tonalitic to granitic rocks that intruded the Punta de Tralca pluton, locally separating it from country rock of the Valparaíso Metamorphic Complex (VMC).

Magmatic foliations and lineations occur in both intrusions. Based on relative age relationships, we were able to distinguish a penetrative older foliation (S_1) and a localized younger foliation (S_2) in the Punta de Tralca tonalite, with a single generation of L_1 lineation associated with the S_1 foliation (Fig. 2B). A single generation of foliation and lineation was observed in the Estero Córdoba granite (S_1, L_1). Foliations in both units generally strike to the NW and dip moderately (~60°) to the NE (Fig. 2B). Lineations defined by stretched enclaves and aligned plagioclase, biotite, and hornblende minerals plunge moderately to steeply (50–60°) toward the northeast. The shared orientation of foliations suggests that the enclaves and their host were comagmatic and exchanged material to varying degrees as they deformed and crystallized. Faulted and folded enclaves, strain shadows of matrix material around xenoliths, and shear zones filled with leucocratic matrix suggest that flattening and near-solidus deformation in a viscous, crystal-rich mush produced the S > L fabric within the Punta de Tralca pluton (Webber et al., 2015). Locally, an Estero Córdoba tonalitic dike records an L > S fabric, and in other places the two units share a common magmatic fabric. Similar orientations of fabric elements in the two units at the regional scale suggest that both record similar bulk flow directions during magma emplacement.

At its southeastern end, the contact between the Estero Córdoba unit and the VMC is characterized by a 15–20 m thick zone of sheeted dikes interfolded with screens of metapelitic and gneissic country rock. The orientations of foliation (S_1) and lineation (L_1) in the VMC units at this locality are similar to those documented in the Punta de Tralca tonalite and the Estero Córdoba granite (Fig. 2B). Stretched and boudinaged dikes are common. Felsic segregations fill the hinges of folds of dikes, suggesting the deformation occurred prior to the complete crystallization of the magma. The dikes include megacrystic granodiorite, granite, and tonalite. Xenoliths of gneiss, slate, metapelitic schist, and calcareous gneiss derived from the host rock are abundant within some of these dikes. The deformation of both the dikes and screens of country rock suggest the Estero Córdoba pluton and the VMC have a shared history of ductile deformation that accompanied magma emplacement.

3.1.2 Microstructures and $^{40}Ar/^{39}Ar$ step-heating results

Sample 11IN01B is from a mafic enclave within the Punta de Tralca unit (Fig. 2D). Continuous S_1 foliation planes within the enclave are composed of dark green and brown hornblende intergrown with elongate, flattened aggregates of plagioclase and quartz. Concentrations of quartz inclusions at plagioclase grain boundaries indicate these two minerals grew together. The aggregates display irregular, amoeboid shapes, indicating the solid-state adjustment of grain boundaries. Plagioclase displays deformation twins. Late biotite overgrew hornblende grains. Small crosscutting fractures are filled with quartz. Step-heating analysis of amphibole from sample 11IN01B resulted in a plateau age of 303.2 ± 1.8 Ma (1σ, including steps comprising 99.5% of the total ^{39}Ar released (Fig. 2C).

Sample 11IN01D is from a biotite- and hornblende-bearing dike that intruded the Punta de Tralca pluton and displays a similar composition and textural features as the Estero Córdoba dike. The mineral assemblage consists primarily of plagioclase, quartz, biotite, and hornblende with minor epidote. Hornblende is locally replaced by chlorite. Plagioclase grains are mostly equant and display only weak alignment. Foliation generally is locally defined by aligned hornblende and biotite, consistent with a dominantly linear (L > S) fabric. Quartz locally exhibits chessboard extinction. Quartz-rich domains display sutured grain boundaries and subgrains, suggesting near-solidus deformation and good grain boundary mobility. Biotite from sample 11IN01D resulted in a more complex spectrum than 11IN01B. The initial low-temperature step gave an age of 202 Ma. The spectrum then climbed to a plateau-like segment that yielded a weighted mean age of 295.7 ± 1.5 Ma, including 59% of the ^{39}Ar released.

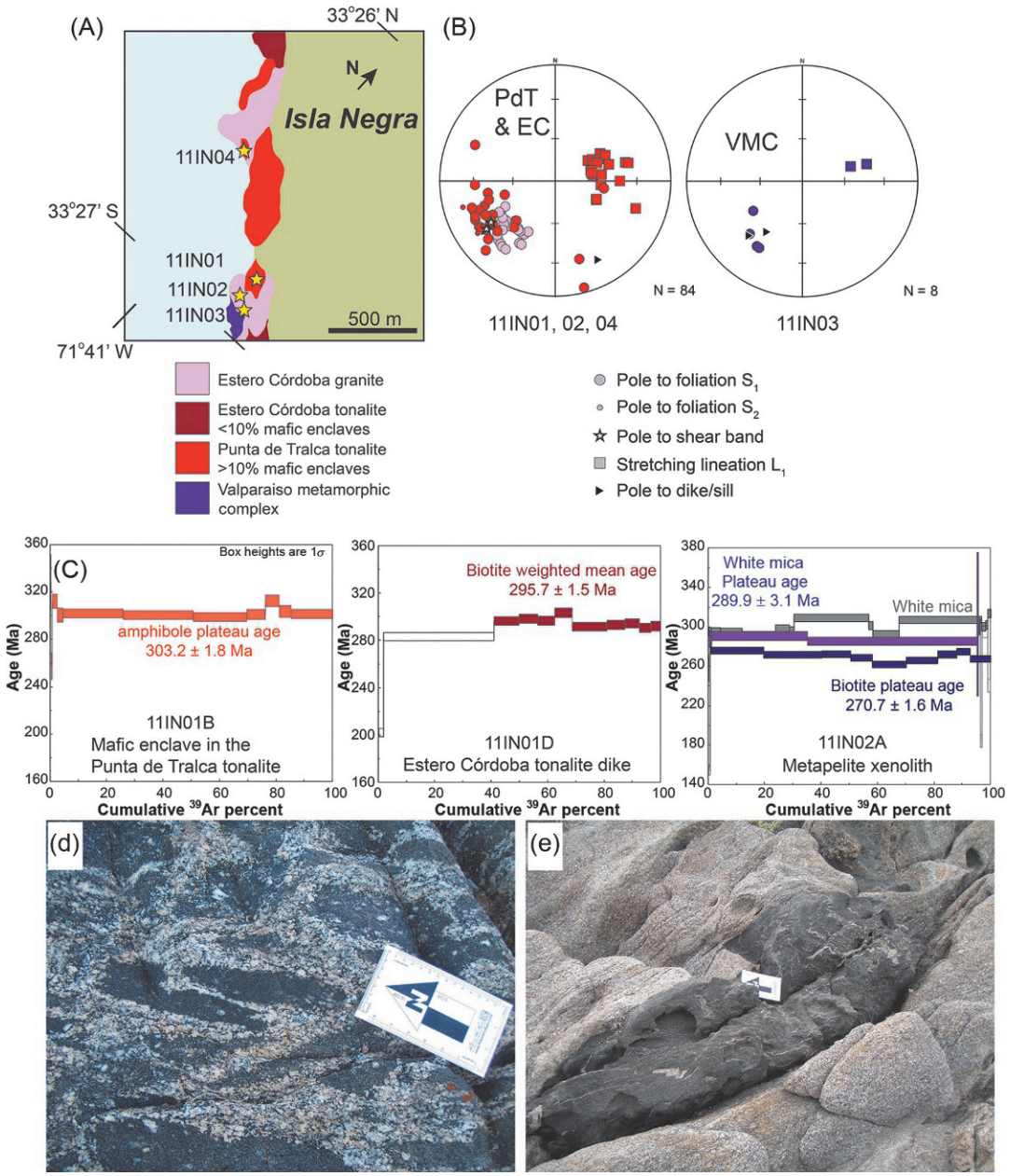

FIG. 2

See figure caption on next page.

Sample 11IN02A is from a metapelitic xenolith within the Punta de Tralca pluton (Fig. 2E). Coarse-grained biotite and muscovite are decussate. Abundant microcline exhibits amoeboid shapes, patchy undulose extinction, and locally displays flame perthite textures. Two aliquots of muscovite and one biotite were analyzed from the metapelite xenolith (11IN02A) in the Estero Córdoba unit. One muscovite analysis resulted in an apparent age gradient: a small (0.1% of the ^{39}Ar released) 228-Ma step followed by a segment of ages c.295 Ma that climb irregularly to a 314-Ma step. A second white mica analysis yielded a plateau age of 289.9 ± 3.1 Ma based on steps comprising 96.2% of the ^{39}Ar released. Biotite from 11IN02A gave an initial minimum age of 154 Ma followed by a 270 ± 1.6 Ma plateau for the vast majority of the gas released.

The 303.2 ± 1.8 Ma amphibole plateau age for sample 11IN01B is interpreted as a minimum age for the timing of intrusion and approximates the timing of deformation documented in outcrop and thin section. Given that 11IN01B and 11IN01D appear to be comagmatic, the younger c. 296 Ma weighted mean age for 11IN01D is consistent with the fact that biotite is generally assumed to have a lower closure temperature to diffusive loss of argon relative to amphibole (McDougall and Harrison, 1999). The xenolith data are a bit more complex. The variable results from muscovite suggest multiple argon reservoirs associated with partial to complete outgassing of the (meta)sedimentary rocks.

3.2 Las Cruces

3.2.1 Field relationships

Near the town of Las Cruces (Figs. 1B and 3A), rocks of the VMC were observed at site 11LC01 and consist of interlayered amphibolite gneiss, calcareous gneiss, and garnet-mica schist. The schist and calcareous gneiss display intrafolial folds and fine-grained hornfels textures. The amphibolite gneiss is migmatitic and garnet-bearing, with patches of variably deformed leucosome. These high-grade (upper amphibolite facies) metamorphic rocks are intruded by garnet-bearing granitic dikes that display gneissic foliations (S_1) defined by coarse plagioclase and potassium feldspar within a fine-grained matrix of biotite, quartz, and hornblende. Both the granitic gneiss and its host rock locally are deformed into tight, upright WNW-trending folds. In most places, S_1 foliation planes strike NW and dip steeply to the NE and SW. Hornblende, feldspar, and biotite mineral stretching lineations (L_1) predominately plunge steeply to the E. These orientations appear throughout the VMC and Santo Domingo Complex, and follow the regional NW-striking structural grain of the old Gondwana continental margin.

Farther west at sites 11LC02-04, fine-grained amphibolite gneisses are hosted within granitic gneiss and biotite granite. Intrusive contacts observed within the quartzo-feldspathic units locally share similar orientations to measured S_1 foliations. At site 11LC03, a small outcrop revealed a sequence in which L > S amphibolite was hosted within an S > L granitic augen gneiss (Fig. 4A). Cross cutting the

FIG. 2, CONT'D

Isla Negra geologic map, structural data, geochronology, and field photos. (A) Geologic map of the Isla Negra area modified from Siña (1987b) with site localities described in the text. (B) Equal-area, lower-hemisphere stereonets of structural data measured at site localities. Data in these stereonets are color coded with respect to rock type; colors are consistent with map units. Abbreviations are as follows: PdT = Punta de Tralca; EC = Estero Córdoba; VMC = Valparaíso Metamorphic Complex. (C) Apparent age spectra resulting from ^{40}Ar/^{39}Ar step-heating analyses. Errors are indicated at the 1σ level. (D) Field photo of mafic enclaves in the Punta de Tralca tonalite in outcrop from which sample 11IN01B was obtained. Long edge of the scale card in the photo is 153 mm. (E) Field photo of the metapelite xenolith (dark rock body) within the Estero Córdoba granite from which sample 11IN02A was obtained.

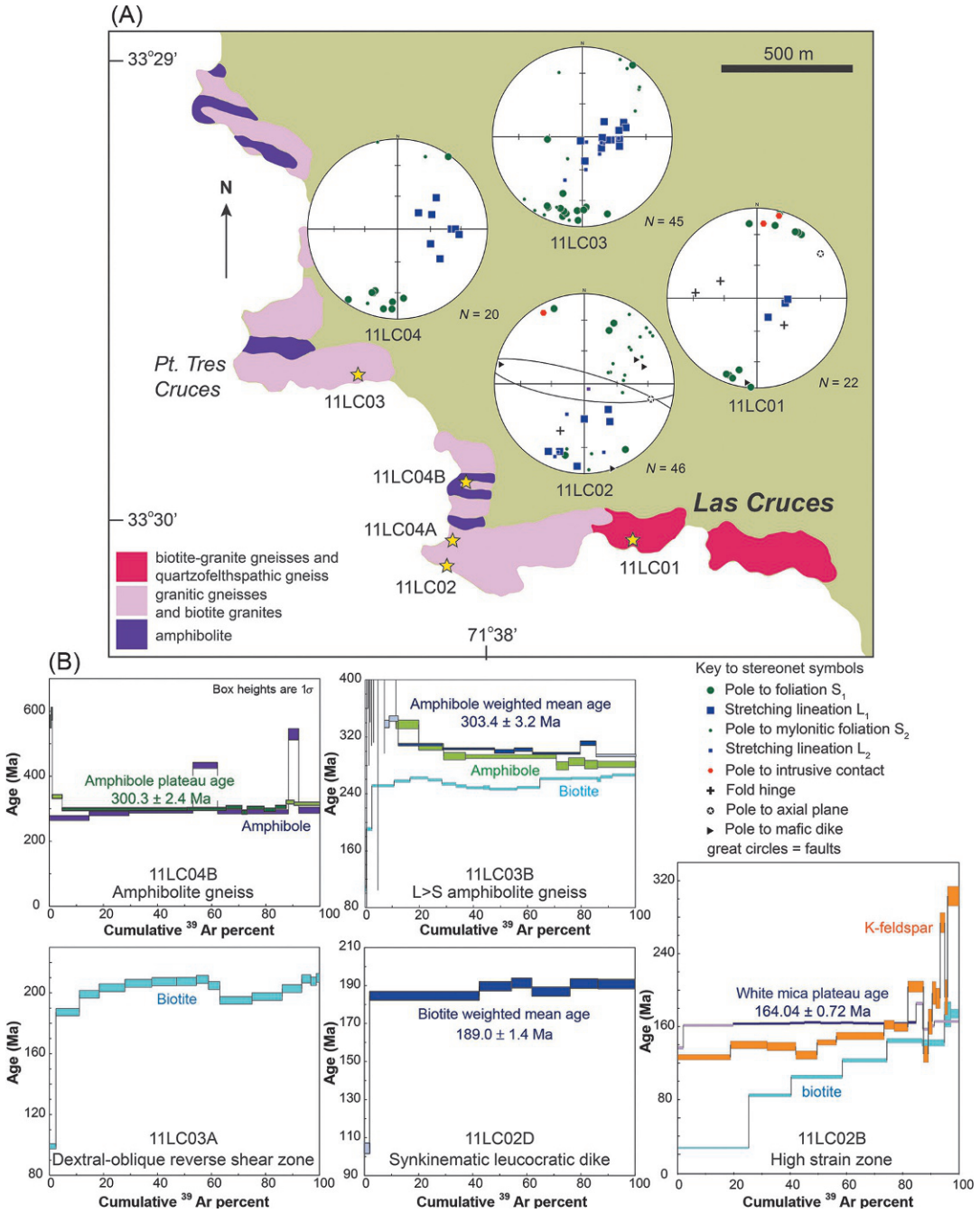

FIG. 3

Las Cruces geologic map, structural data, and geochronology. (A) Geologic map of the Las Cruces area modified from Siña (1987b) with site localities described in the text. Structural data recorded at each site are shown in equal-area, lower-hemisphere stereonets. (B) Apparent age spectra resulting from of $^{40}Ar/^{39}Ar$ step-heating analyses. Errors are indicated at the 1σ level.

granitic augen gneiss is a series of thin (10–25 cm) mylonitic to ultramylonitic shear zones. Mylonitic foliations (S_2) all strike to the northwest and dip variably to the NE and SW. Some appear folded about WNW-trending folds. All of the shear zones record a top-to-the-NE sense of shear parallel to NE- and SW-trending mineral stretching lineations (L_2). Their orientations and kinematics of the shear zones all are compatible with NE-SW shortening and reverse motion with a small component of dextral shear. Leucocratic veins and dikes, some garnet-bearing, intruded the shear zones (Fig. 4A and B). Some of the dikes cut the mylonitic foliation but also are folded within the shear zones. The axial planes of the folds parallel mylonitic foliation planes outside the dike margins, indicating that the dikes were emplaced after shearing began but before the deformation ended. A younger suite of moderate-to-steeply dipping mafic dikes with variable strikes cross cut both the leucocratic dikes and the mylonites. Locally, steeply dipping WNW-striking cataclastic faults crosscut all of the foregoing and display minor offsets.

3.2.2 Microstructures and $^{40}Ar/^{39}Ar$ step-heating results

Sample 11LC04B is an amphibolite gneiss (S_1, L_1) hosted within a granitic augen gneiss. The primary mineral assemblage includes interlocking grains of orthopyroxene, oxyhornblende, plagioclase, Fe-oxides, and minor quartz. Orthopyroxene is altered internally along fractures to iddingsite and to fine-grained mats of calcic amphibole along grain boundaries shared with plagioclase. The alteration to calcic-amphibole appears to be concentrated fractures that cut the rock and likely served as fluid pathways. Two aliquots of amphibole from 11LC04B were analyzed. One aliquot yielded a plateau age of 300.3 ± 2.4 Ma (Fig. 3B). The second aliquot resulted in a more complex spectrum dominated by an age gradient from 271 Ma to 296 Ma with increasing temperature of gas extraction.

Sample 11LC03B is the L>S amphibolite gneiss (S_1, L_1). In thin section, this sample exhibits a fine-grained interlocking assemblage of hornblende, biotite, plagioclase, and orthopyroxene. The thin section preserves a cross-cutting leucocratic vein. Both the amphibolite and vein are crosscut by a brittle fracture. Two aliquots of amphibole were analyzed, with one yielding a weighted mean age of 303.4 ± 3.2 Ma. The second aliquot resulted in a spectrum with decreasing ages produced by increasing temperatures of extraction, with a minimum age c. 280 Ma. Step-heating of biotite resulted in a complex spectrum dominated by an age gradient from c.250 to 267 Ma over ~90% of the ^{39}Ar released. The lowest temperature steps resulted in ages c.108 and 191 Ma.

Sample 11LC03A is from the margin of the mylonitic dextral-oblique reverse shear zone (S_2) that cuts the granitic augen gneiss hosting the 11LC03B amphibolite. The thin section captures the zone intruded by leucocratic veins during shearing. Garnet porphyroclasts are altered to biotite along their margins and in fractures. Quartz ribbons associated with leucocratic melts entrain biotite grains and display chessboard extinction (Fig. 3B). Quartz domains include amoeboid grains that show evidence for grain boundary migration. Plagioclase and K-feldspar grains display core mantle structures, and are associated with myrmekite, deformation twins, and flame perthite. Step-heating of biotite resulted in a spectrum dominated by an apparent age gradient from 187 to 210 Ma over ~89% of the ^{39}Ar released. The minimum age at the lowest temperature step is c.99 Ma.

Sample 11LC02D is a synkinematic leucocratic dike that displays mylonitic deformation (S_2). Its microstructures bear resemblance to 11LC03A: garnet porphyroclasts altered to biotite, quartz ribbons with chessboard extinction, and K-feldspar grains with core-mantle structures and flame perthite. Locally within the thin section, biotite grains are decussate. Step-heating of biotite from this sample yielded a plateau-like segment with a weighted mean age of 189.0 ± 1.4 Ma. However, we note an apparent age-gradient in these steps from c. 185 to 191 Ma. The lowest temperature step is associated with a minimum age of c.104 Ma.

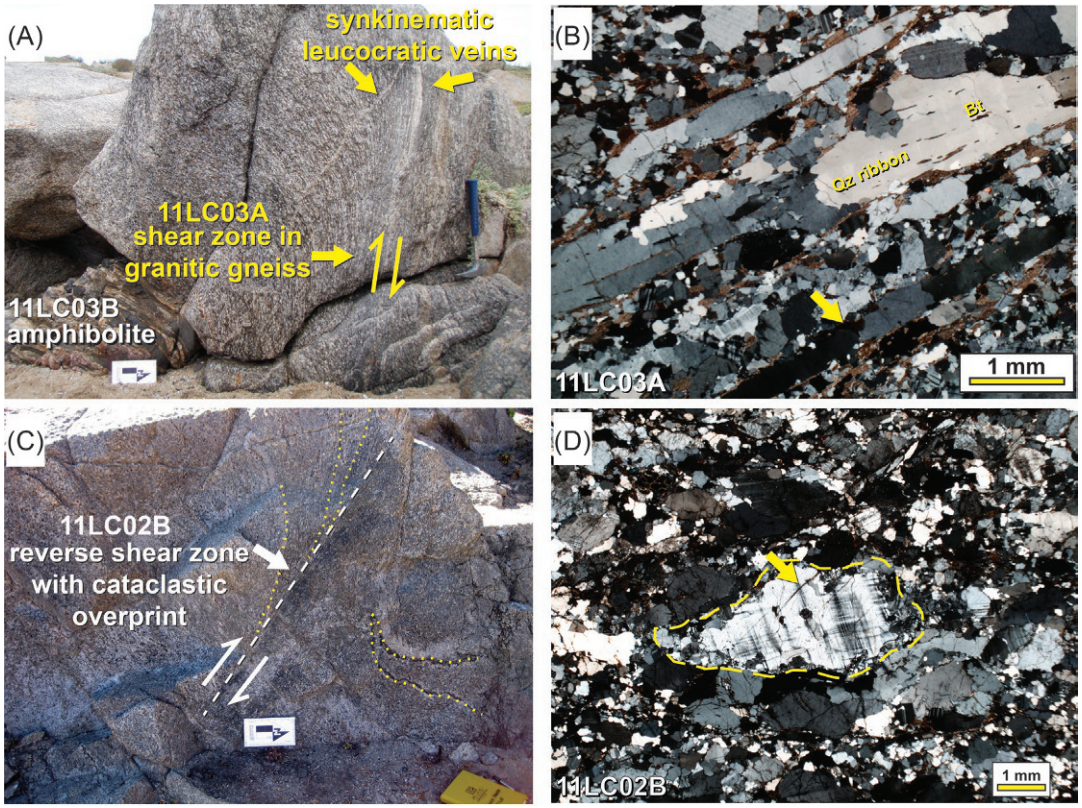

FIG. 4

Field photos and photomicrographs from Las Cruces area. (A) Photo of L > S amphibolite hosted in garnet-bearing granitic gneiss that is deformed by a reverse shear zone associated with leucocratic veins. Estwing rock hammer shown for scale. (B) Photomicrograph of sample 11LC03A (shown in A). Quartz (Qz) ribbons that entrain biotite (Bt) grains and display chessboard extinction are inferred to be related to leucocratic melts that intruded foliation planes *(yellow arrow)*. (C) Field photo of 11LC02B high-strain zone associated with apparent reverse shear; kinematics inferred from deflection of foliations into shear zone and drag (re)folding of a mafic layer *(dotted yellow lines)*. Long edge of the scale card in the photo is 153 mm. (D) Photomicrograph of sample 11LC02B showing K-feldspar with core-mantle structure. The *dashed yellow line* denotes outer edge of the mantle. The *yellow arrow* points to a microfracture within the K-feldspar grain.

Sample 11LC02B is from a high strain zone (S_2) in the vicinity the mafic dikes described earlier and is associated with an apparent reverse shear zone in garnet-bearing granitic gneiss (Fig. 4C). In thin section, K-feldspar show core-mantle structures and are associated with myrmekite (Fig. 4D). White mica locally is associated with very fine leucocratic veins. A strong cataclastic overprint is apparent in thin section, including shredded biotite grains and microfractures in feldspars. Step-heating of K-feldspar and biotite resulted in age gradients from 126 to 303 Ma and 28 to 174 Ma, respectively. In comparison, the white mica yielded a relatively flat spectrum with a plateau age of 164.04 ± 0.72 Ma.

3.3 Agua Salada

3.3.1 Field relationships

Coastal exposures between Cartagena and San Antonio, referred to here as Agua Salada (Figs. 1B and 5A), consist of locally migmatitic orthogneisses (Fig. 6A) intruded by multiple generations of amphibolite and granitic dikes. At 11AS01, tonalitic orthogneiss displays a penetrative NE- and E-striking S_1 foliation associated with a moderately plunging SW-trending L_1 lineation. The S_1 foliations are folded and cut by arrays of sinistral shear bands. The shear bands are steep, strike to the NW (Fig. 5A), and show offsets of only a few to tens of centimeters (Fig. 6B). Most of the shears contain unfoliated veins of quartz-rich leucosome in their centers. Unfoliated leucocratic veins are locally concordant with the orthogneiss foliation. The mafic dikes that intrude the granodioritic gneiss are open to tightly folded and stretched. Most are disharmonic and ptygmatic, and many are cut and surrounded by leucosome, especially where they have broken apart to form boudins. These relationships suggest that the folding and stretching of the mafic dikes, along with formation of the minor shear zones, all occurred in the presence of melt. Late, granitic veins and dikes cut across the amphibolite dikes, indicating that melts continued to migrate through the rock after deformation mostly had ceased. Some granitic dikes are cut by brittle faults showing offsets of a few centimeters.

High strain zones associated with S_1 foliations are especially evident at sites 11AS02 and 11AS03. In these areas, migmatitic textures in the granitic host gneiss are rare to absent at outcrop scale. High strains are indicated by tight-isoclinal folds of amphibolite dikes, few discordant dikes, K-feldspar augen with long tails, and the presence of well-developed biotite and quartz mineral stretching lineations (L_1). Mineral lineations (L_1) in these high strain zones plunge moderately to the SW on steep S_1 foliation planes that strike to the ENE. Some asymmetric pressure shadows of biotite around of K-feldspar augen also are present. These asymmetric structures record both dextral and sinistral shear senses. The dominant shear sense appears to be top-down-to-the-SW (dextral-normal), parallel to the SW-plunging L_1 mineral lineations.

3.3.2 Microstructures and $^{40}Ar/^{39}Ar$ step-heating results

Sample 11AS01A is an amphibole and biotite-rich tonalitic gneiss (S_1, L_1) intruded by leucocratic veins; both are ptygmatically folded. A thin section of 11AS01A captures the contact between a leucocratic vein and the gneiss (Fig. 6C). The gneiss preserves an assemblage of decussate amphibole and biotite, plagioclase and minor quartz. The gneiss exhibits evidence for brittle fractures locally near the vein contact in association with alteration of amphibole and biotite (Fig. 6C). Quartz in the leucocratic vein displays chessboard extinction and records evidence for dynamic recrystallization by grain boundary migration. Locally, feldspars in the veins have deformation twins. Two small aliquots (1–2 grains) of amphibole and one aliquot of biotite were analyzed by step-heating. One amphibole aliquot yielded a plateau age of 215.6 ± 1.4 Ma, with some minor disturbance at the low-temperature steps (Fig. 5B). A second amphibole aliquot yielded a more complicated spectrum principally characterized by serially increasing ages at low temperature steps that climb to a plateau-like segment yielding a weighted mean age of 211.8 ± 1.4 Ma. The minimum age obtained from this amphibole is consistent with the 157.29 ± 0.79 Ma plateau age obtained from the biotite. The biotite apparent age spectrum also showed increasing apparent ages over the initial ~15% of the ^{39}Ar released before plateauing.

Sample 11AS01B shares similar outcrop and thin-section characteristics to 11AS01A, with the exception that amphibole and biotite locally appear more corroded. Microfractures are observed crosscutting the rock near the boundary with the leucocratic vein in this thin section (Fig. 6C). The step-heating

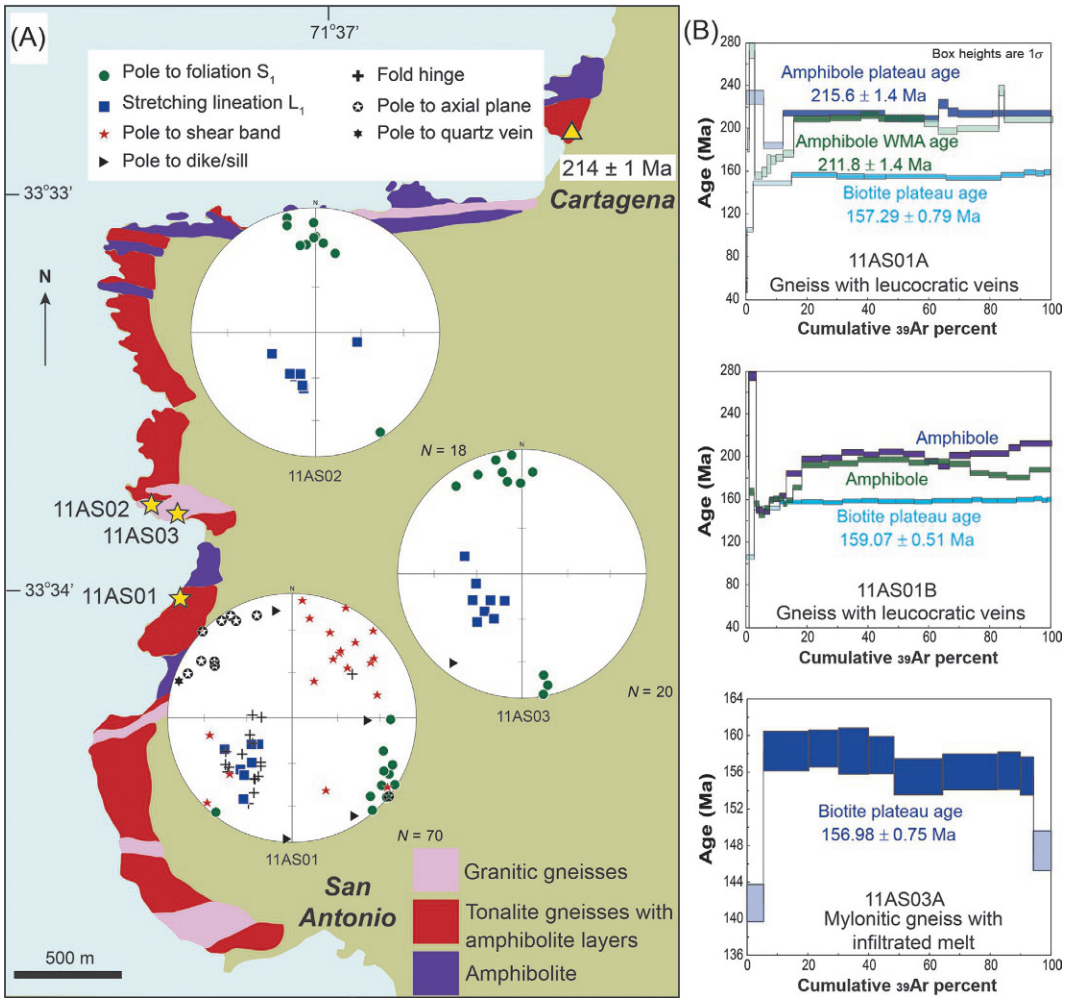

FIG. 5

Agua Salada geologic map, structural data, and geochronology. (A) Geologic map of the Agua Salada area modified from Siña (1987b) with site localities described in the text. Structural data recorded at each site are shown in equal-area, lower-hemisphere stereonets. (B) Apparent age spectra resulting from of $^{40}Ar/^{39}Ar$ step-heating analyses. Errors are indicated at the 1σ level.

analyses of amphibole and biotite also yielded similar results to those obtained from 11AS01A except that the amphibole spectra are more disturbed. Both amphiboles record age gradients; minimum ages are roughly consistent with the biotite plateau age of 159.07 ± 0.51 Ma. One amphibole then climbs to a maximum age c. 212 Ma, the other climbs to c.196 Ma. The biotite plateau comprises 89% of the ^{39}Ar released. Younger steps from lower temperatures of release include a minimum age of c.106 Ma.

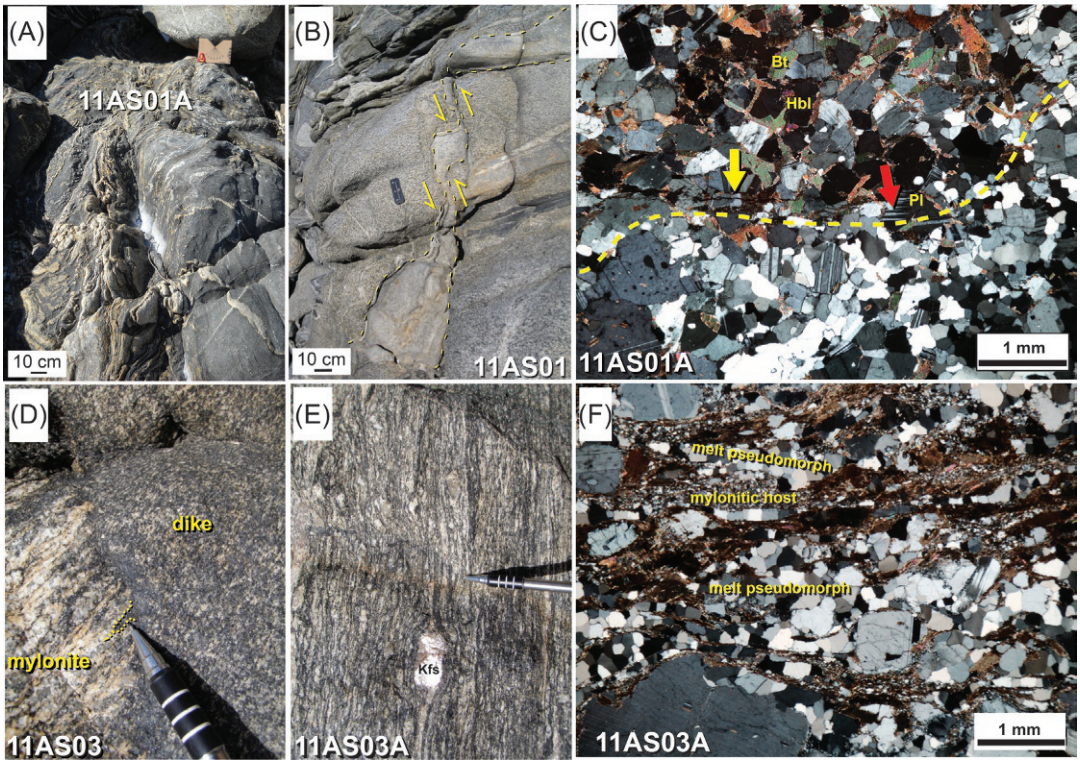

FIG. 6

Field photos and photomicrographs from Agua Salada. (A) Migmatitic gneiss (11AS01A) with ptygmatic leucocratic veins. (B) Syntectonic dike at site 11AS01 showing boudinage associated with sinistral offsets. (C) Photomicrograph of sample 11AS01A that captures the boundary between the gneiss and leucocratic vein; the boundary is denoted by the *dashed line*. Hornblende (Hbl) grains appear black, and together with biotite (Bt) and plagioclase (Pl) and minor quartz represent gneiss displaying the S_1/L_1 structural elements described in text and shown in Fig. 5A. Approximate boundary between the leucocratic vein and gneiss is associated with microfractures *(yellow arrow)* and deformation twins in plagioclase *(red arrow)*. (D) Field photo from site 11AS03 showing a close up of the margin of a syntectonic dike. The tip of the mechanical pencil points to one of the tapered dike lobes *(dashed yellow line)* that infiltrates foliation planes in the host mylonite. (E) Field photo of the host mylonite with large K-feldspar (Kfs) porphyroclasts. (F) Photomicrograph of sample 11AS03A, the mylonite intruded by the dike shown in (D). The mylonitic host is locally ultramylonitic and represented by rafts of biotite-rich fine grained material between domains of polygonal quartz that represent pseudomorphs of the melt that infiltrated along foliation planes.

Sample 11AS03B comes from mylonitic granitic gneiss (S_1, L_1) proximal to a crosscutting leucocratic dike (Fig. 6D and E). Based on outcrop observations, melt from the dike infiltrated foliation planes within the host gneiss. The former melt in thin section is represented by polygonal, strain-free quartz grains, networks of which entrain mylonitic and ultramylonitic host rock material (Fig. 6F). Step-heating of biotite from this sample yielded a plateau age of 156.98 ± 0.75 Ma. The plateau is

bounded by younger ages obtained from both the lowest and highest temperature steps. The minimum age obtained from this sample is c. 146 Ma.

3.4 Quintay

3.4.1 Field relationships

Coastal outcrops near the town of Quintay form part of a NW-trending belt of Middle-Late Jurassic rocks that intrude the Carboniferous-Permian batholiths exposed farther south (Fig. 1B). The Jurassic rocks consist mainly of tonalitic, dioritic, and granitic gneisses intruded by mafic dikes. The igneous rocks display gneissic foliations (S_1) that mainly strike to the NW and dip steeply to the SW and NE (Fig. 7C), parallel to the regional trend of the batholith. Most mineral lineations (L_1) have steep to subvertical plunges. Clusters of fine-grained mafic enclaves in dioritic gneiss locally define an igneous flow banding and are surrounded by granitic segregations. Amphibolite layers up to 3 m thick cut through the gneisses and are foliated, indicating that deformation outlasted magma emplacement at the southern end of the batholith.

Superimposed on the S_1 gneissic foliations within the Jurassic batholith are steep high strain zones that mostly strike to the NW and are similar in both orientation and style as the melt-infiltrated shear bands observed at Agua Salada. These shear zones display mineral stretching lineations composed of quartz, biotite, hornblende, and K-feldspar that plunge steeply and moderately to the NW, SW, and SE. The deflection of gneissic fabrics into these shear zones, asymmetric shear bands composed of biotite, and numerous asymmetric porphyroclasts indicate that the high strain zones record reverse and sinistral-oblique shear senses. Late dextral faults that strike to the NW cut across all ductile shear zones.

3.4.2 Microstructure and radiometric age constraints

Sample 11QT01A was obtained from a high strain zone in a granitic gneiss with K-feldspar augen consistent with top-to-the-NE reverse shear sense along foliation planes striking NW and dipping steeply to the SW. The K-feldspar augen in thin section is mantled with myrmekite grains and locally display flame perthite. Quartz ribbons exhibit chessboard extinction and quartz domains preserve grain boundary migration microstructures.

We did not obtain any $^{40}Ar/^{39}Ar$ data from Quintay. A U-Pb zircon age of 168.9 ± 1.4 Ma was published by Deckart et al. (2014) for a quartz-bearing gabbro from the same suite of outcrops observed in our study.

4 Discussion

4.1 Late Carboniferous-Early Permian arc magmatism and deformation

The plateau and weighted mean $^{40}Ar/^{39}Ar$ amphibole and biotite ages from samples 11IN01B and 11IN01D (Fig. 2C) establish a ~300 Ma age for the igneous Santo Domingo Complex at Isla Negra. This determination is slightly older than Early Permian U-Pb zircon ages obtained by Berg and Charrier (1987), Godoy and Loske (1988), and Hervé et al. (1988), and slightly younger than the Late Carboniferous U-Pb zircon ages reported by Deckart et al. (2014). In addition, small differences in mineral ages between the two samples allow us to infer that the Late Carboniferous batholith was constructed relatively quickly from the incremental emplacement of multiple batches of magma. The older 303.2 ± 1.8 Ma $^{40}Ar/^{39}Ar$

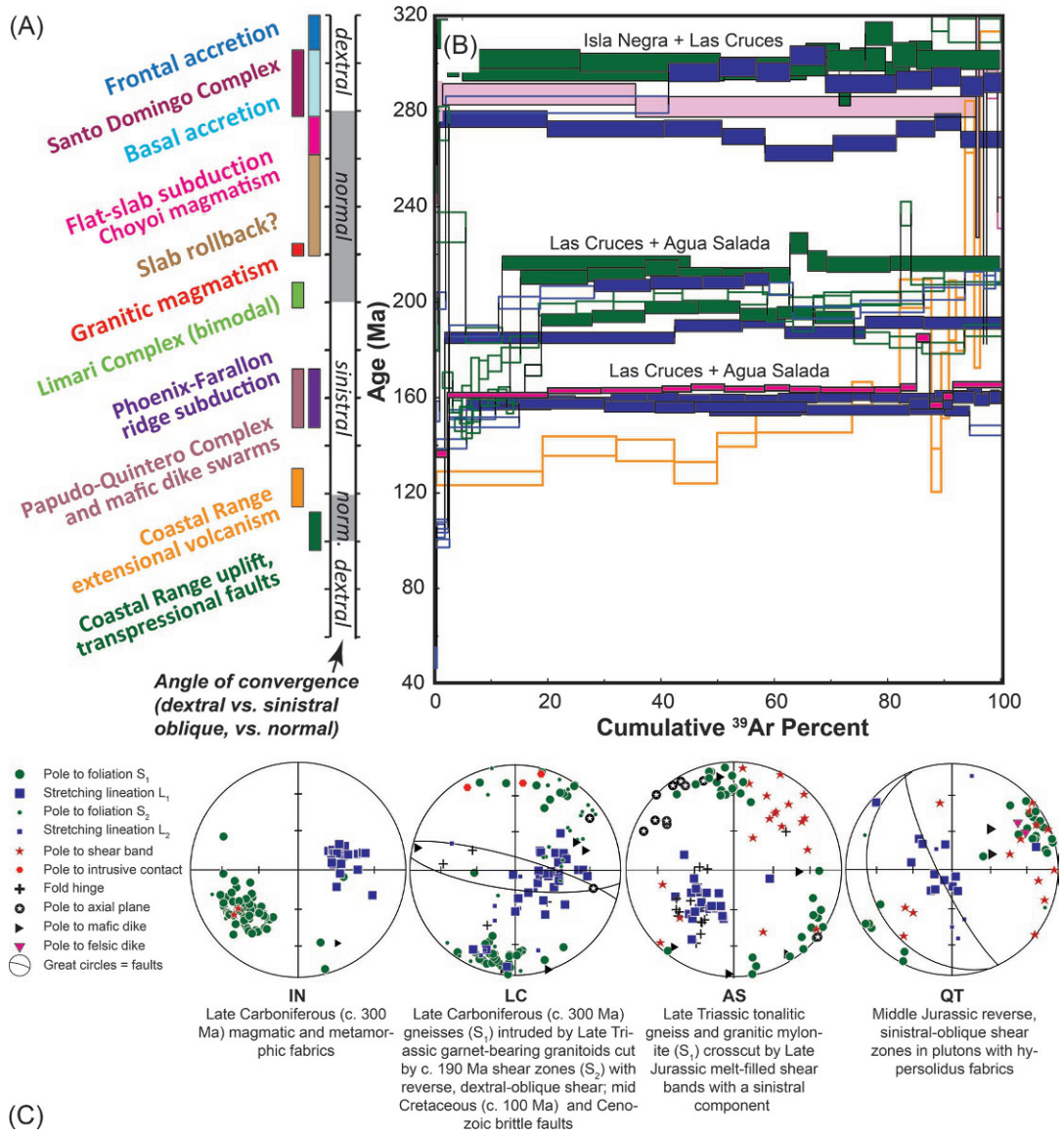

FIG. 7

Summary figure of geochronology and structural data presented in this manuscript. (A) Timeline summarizing key tectonic and igneous events documented regionally (summarized from Creixell et al., 2006, 2009, 2011; Kleiman and Japas, 2009; Parada et al., 1999; Richter et al., 2007; Vásquez et al., 2011; Willner et al., 2005, 2009, 2012). In the timeline, "dextral," "normal," and "sinistral" refer to the dominant plate motion vector component during oblique or normal convergence inferred from plate reconstructions of Domeier and Torsvik (2014) and Seton et al. (2012). Timeline shares a common age axis with the composite apparent age spectra diagram. (B) Composite apparent age spectra plot for all $^{40}Ar/^{39}Ar$ data highlights clustering of ages, both in terms of plateau or plateau-like segments as well as minimum ages such as those c.100 Ma. (C) Composite stereonets for each location discussed in text with summary of interpretations. IN = Isla Negra, LC = Las Cruces, AS = Agua Salada, and QT = Quintay.

amphibole age obtained from a mafic enclave within the Punta de Tralca pluton (sample 11IN01B) and the slightly younger 295.7 ± 1.5 Ma $^{40}Ar/^{39}Ar$ biotite age from the Estero Córdoba dike (sample 11IN01D) show that the dike intruded shortly after the pluton was emplaced. This result, combined with the preservation of high-temperature microstructures indicating both magmatic and solid-state deformation, suggests that both units interacted comagmatically and cooled relatively quickly. Early Permian white mica and biotite $^{40}Ar/^{39}Ar$ cooling ages (289.9 ± 3.1 Ma and 270.7 ± 1.6 Ma, respectively) from sample 11IN02A support this interpretation, while also showing that the enclaves and xenoliths (Fig. 2E and D) within the Punta de Tralca pluton reflect multiple sources. Together, the data support the conclusions of Webber et al. (2015) who suggested that the Santo Domingo Complex was constructed by the injection of intermediate magmas as dikes into viscous, crystal-rich mushes, which mobilized felsic melts and drove them upward and outward toward the roof and margins of the system.

Structural observations made near the southern contact between the Estero Córdoba unit and the Valparaíso Metamorphic Complex at Isla Negra suggest that these two units also have a shared history of deformation that accompanied magma emplacement. The oldest suite of structural elements (S_1/L_1) at Isla Negra are observed in the calcsilicate gneisses of the Valparaíso Metamorphic Complex and amphibolites, showing similar trends as those observed in igneous rocks inside the Santo Domingo batholith (Figs. 2B and 3A). The amphibolites (samples 11LC04A and 11LC03B) with igneous origins inferred on the basis of petrographic observations yielded Late Carboniferous $^{40}Ar/^{39}Ar$ amphibole ages of ~300 Ma, similar to the ages obtained from the Santo Domingo Complex (Fig. 3B). This structural and geochronologic concordance suggests that dikes and magmatic sheets exploited a regional structural grain that strikes to the NW and dips moderately to the NE, and that the regional NW-striking structural grain of the coastal Andes had formed by Late Carboniferous time during a period of subduction, arc magmatism, and accretion (Fig. 7A–C).

4.2 Late Triassic-Early Jurassic granitoids, leucocratic intrusions, and high-strain shear zones

In the Las Cruces region, the VMC and Late Carboniferous-Early Permian arc rocks are intruded by a suite of garnet-bearing granitic gneisses crosscut by steeply dipping reverse shear zone associated with synkinematic leucocratic intrusions. The strongest age signal associated with the high-strain S_2/L_2 structural elements is c. 190 Ma based on the $^{40}Ar/^{39}Ar$ biotite weighted mean age from 11LC02D and the younger steps in Triassic-Jurassic apparent age gradient obtained from 11LC03A biotite (Fig. 4B). A Triassic age of intrusion of the garnet-bearing gneisses at Las Cruces is inferred from the above (i.e., older than 190 Ma) and a maximum age constrained at c.250 Ma from the biotite $^{40}Ar/^{39}Ar$ apparent age gradient from 11LC03B, which is the amphibolite hosted by the granitic gneiss. Because of the local preservation of Late Carboniferous $^{40}Ar/^{39}Ar$ ages and microstructures, the high-temperature microstructures (e.g., chessboard extinction in quartz, feldspar core-mantle structures with myrmekite) observed in 11LC03A are inferred to be related to the influx of melt into the shear zone as opposed to reflecting high ambient crustal temperatures.

Amphiboles analyzed from tonalite gneiss hosting leucocratic melts at site 11AS01 yield Late Triassic plateau or plateau-like segments that are variably disturbed and show age gradients (Fig. 5B). The 11AS01A amphibole plateau age of 215.6 ± 1.4 Ma is concordant with a 214 Ma U-Pb for zircon from diorite gneisses farther north near Cartagena reported by Gana and Tosdal (1996). The E-W striking foliations observed in the host gneiss and mylonites in our study are shared by the coastal basement rock

exposures from Cartagena to San Antonino (Fig. 5A). Therefore, we infer that the E-W-striking foliations in tonalite gneisses and granitic mylonites at Agua Salada formed in the Late Triassic at c.215 Ma.

Overall, the Late Triassic ages inferred for the granitic gneisses and mylonites, and Early Jurassic ages associated with shear zones and syntectonic leucocratic intrusions are consistent with documented pulses of felsic magmatism regionally (e.g., Vásquez et al., 2011; Parada et al., 1999). The timing of these events roughly coincided with late stages of slab rollback (Parada et al., 1999) following a period of flat slab subduction (Kleiman and Japas, 2009) and the transition from normal convergence to oblique convergence, respectively (Domeier and Torsvik, 2014; Seton et al., 2012) (Fig. 7A and B).

4.3 Late Jurassic arc magmatism and deformation

Late Jurassic syntectonic intrusions are documented at Las Cruces, Agua Salada, and Quintay. Hypersolidus and solid-state deformation within the Jurassic plutons at Quintay most likely record multiple pulses of magmatism and deformation during growth of the pluton. In contrast, Jurassic shear zones at Las Cruces and Agua Salada are more localized, with clear finite cm-dm-scale offsets apparent at Agua Salada. The $^{40}Ar/^{39}Ar$ data obtained from 11LC02B associated with a reverse shear zone suggest the protolith of this metamorphic tectonite may be Carboniferous (~303 Ma maximum age; Fig. 3B). Based on microstructural observations, the 164.04 ± 0.72 Ma white mica plateau age appears to be associated deformation in the presence of fluid/melt. This age falls within the range of U-Pb ages reported for the Jurassic plutons near Quintay (Fig. 1B) (Godoy and Loske, 1988; Deckart et al., 2014) in which reverse sinistral-oblique shear zones are documented (Fig. 7C).

At Agua Salada, the $^{40}Ar/^{39}Ar$ amphibole age gradients from the tonalitic gneisses at 11AS01 in some case correlate strongly with the Late Jurassic biotite plateau ages obtained from the same samples (c.157 and 159 Ma; Fig. 5B). The thin sections suggest that these Late Jurassic ages record the timing of leucocratic melt infiltration (Fig. 6C). This interpretation also is supported by the biotite age obtained from 11AS03A, in which melt from a syntectonic dike can be traced in outcrop (Fig. 6D) and seen in thin section (Fig. 6F) infiltrating foliation planes of the inferred Late Triassic mylonite. The NW-striking shear bands associated with small-scale apparent sinistral offsets (Figs. 5A and 6B) of leucocratic veins and syntectonic dikes represent a discrete pulse of melt-enhanced deformation in the Late Jurassic. Similar to the earlier argument for Las Cruces, because of the local preservation of Late Triassic $^{40}Ar/^{39}Ar$ ages and microstructures, the influx of the leucocratic melts and associated shearing is inferred to have occurred at mid-upper crustal levels.

The Late Jurassic biotite $^{40}Ar/^{39}Ar$ ages of 157–159 Ma from Agua Salada are concordant with ages reported for mafic dike swarms at Concón and Cartagena (Fig. 1B) reported by Creixell et al. (2006, 2009, 2011). Through integrated structural and geochronological studies, including comparisons with Early Cretaceous dikes near El Tabo, these authors documented alternating episodes of sinistral transtension and transpression across NW-WNW-striking structures during construction of the Jurassic magmatic arc. The timing of these events suggests they may relate to processes associated with Phoenix-Farallon ridge subduction (Fig. 7A).

4.4 Cretaceous (and younger) faulting

Within at least four samples analyzed, including samples 11LC03A and 11LC02D from Las Cruces (Fig. 3B) and samples 11AS01A and 11AS01B from Agua Salada (Fig. 5B), biotite age spectra

show minimum ages ranging from ~106 to 99 Ma at the lowest temperature step. In each of the sites sampled, late brittle reverse and dextral strike-slip faults cross cut all dikes and shear zones in the rocks sampled, showing small offsets and cataclastic textures. We interpret these minimum ages to be significant and to reflect a mechanical resetting of the biotite spectra rather than a thermal resetting of this mineral. The large section of the Chilean coast affected by this pattern suggests that it reflects a regional faulting event at ~100 Ma that was not associated with magmatism, melting or a major thermal pulse. These characteristics all are consistent with a period of Coastal Range uplift and dextral and dextral-reverse faulting affecting the shallow crust of the fore-arc during mid-Cretaceous times (Fig. 7B).

Dextral and dextral-reverse faults similar in style and age as those described earlier also have been observed elsewhere in the Coast Ranges, including in the Silla del Gobernador shear zone (SGSZ in Fig. 1A) (Arancibia, 2004). A similar age of deformation is documented for the left-lateral Pichilemu-Vichuquén Fault farther south (PVF in Fig. 1A) (Willner et al., 2009). All of these structures formed during a period of mid-Cretaceous compression that followed an older cycle of Jurassic-Early Cretaceous extension and transtension within the margin (Dalziel, 1981; Mpodozis and Ramos, 1989; Ramos and Folguera, 2005; Cembrano et al., 2005). This onset of mid-Cretaceous compression coincided with an increase in the trench-normal absolute velocity of the overriding plate (Maloney et al., 2013), which caused shortening and uplift within the Andes, including in the forearc region (Horton, 2018, and references therein).

5 Conclusions

New structural and $^{40}Ar/^{39}Ar$ geochronology establish that a widely recognized regional NW-WNW-striking structural grain that crosscuts the Coastal Ranges oblique to the current continental margin formed during the Late Carboniferous when subduction initiated beneath Gondwana and a magmatic arc was emplaced. This age is significantly older than those previously postulated and establishes its origin. In the study area, the arc is represented by the Santo Domingo Complex and shows multiple magmatic foliations that strike to the NW and dip moderately (~60°) to the NE. Small differences in the mineral ages of sampled rocks from the batholith (303.2 ± 1.8 to 295.7 ± 1.5 Ma) suggest that the arc was constructed relatively quickly from the incremental emplacement of multiple batches of magma.

Since its inception in the Late Carboniferous, the regional structural grain appears to have influenced most subsequent phases of deformation and magmatism in the Coast Ranges during periods of oblique convergence, including during the formation of the modern Andean plate boundary. Between 33°S and 34°S latitude, the new data reported here show at least two distinctive phases of Early and Late Jurassic melt-enhanced deformation that record displacements on NW-striking structures.

In the Agua Salada region, migmatitic tonalite gneiss displays penetrative NE- and E-striking steeply dipping foliations and SW-trending lineations with moderate plunges. Existing geologic maps indicate that these structural trends are shared by rocks along the coast between San Antonio and Cartagena, including mylonitic shear zones in granitic lithologies. We infer these structures to have formed at c.215 Ma based on $^{40}Ar/^{39}Ar$ data from amphibole and a published U-Pb zircon age.

The Late Triassic structures at Agua Salada are folded and cut by arrays of steep sinistral shear zones that strike to the NW. We interpret the shear bands to be coeval with the infiltration of melt along older foliation planes during the Late Jurassic (159–157 Ma). The timing of this latter event is similar

to those reported for the emplacement of mafic dike swarms during construction of a Jurassic arc at Concón and Cartagena.

In the Las Cruces region, Early Carboniferous-Permian arc rocks were intruded by a suite of garnet-bearing granitic gneisses cut by steeply-dipping reverse shear zones into which granitic intrusions were emplaced at ~190 Ma. These shear zones all strike to the NW, dip variably to the NE and SW, and record top-to-the-NE reverse displacements.

Overall, the Late Triassic and Early Jurassic ages associated with shear zones and syntectonic leucocratic intrusions at Las Cruces and Agua Salada are consistent with regional pulses of felsic magmatism. The timing of these events approximately coincides with stages of slab rollback following a period of flat slab subduction and the transition from normal convergence to oblique convergence, respectively.

Late Jurassic magmatism and deformation is variably manifest at Quintay, Las Cruces, and Agua Salada, where sinistral-oblique deformation is associated with magmatism and melt infiltration. Quintay preserves evidence for both hypersolidus and solid-state deformation during the progressive construction of the Late Jurassic magmatic arc. In contrast, the melt-filled shear zones with strain-free melt pseudomorphs preserved in thin section appear to represent a single increment of melt-enhanced deformation.

A brittle phase of deformation, inferred to have occurred at ~100 Ma, is present in all localities studied. This phase also formed NW-WNW-striking cataclastic faults in outcrop and as microfaults in thin section. Its inferred age is based on the minimum ages of argon-loss profiles and may correlate with high-strain ductile and cataclastic shear zones documented north of the study area.

This study demonstrates that multiple episodes of deformation in the Coast Ranges were inextricably linked to pulses of subduction-related magmatism and, during times of oblique convergence, reactivated a late Paleozoic NW structural grain that dominates the Andean margin. Comparison of our results with published data from farther south indicates our study area may provide insight into modern deformation in the mid-lower crust in the Pichilemu region where reactivation of NW-striking structures in the middle crust occurs during coseismic deformation in the upper plate of the Chile subduction zone. Similar potential may exist for active faults in the Valparaiso region that share the long-lived NW-striking structural trend.

Acknowledgments

We gratefully acknowledge Drs. José Cembrano, Diego Morata, and Gloria Arancibia for many discussions, insights, and assistance. Jeffrey Webber and Gabriela Mora-Klepeis helped with fieldwork and contributed discussions. Daniel Jones provided expertise and assistance with the argon analyses. Funding for fieldwork was provided partly by NSF grant EAR 063594 to K. Klepeis.

Appendix: Supplementary material

Supplementary material related to this chapter can be found on the accompanying CD or online at https://doi.org/10.1016/B978-0-12-816009-1.00020-4.

References

Aguirre, L., Hervé, F., Godoy, E., 1972. Distribution of metamorphic facies in Chile, an outline. Kristalinikum 9, 7–19.

Arancibia, G., 2004. Mid-Cretaceous crustal shortening: evidence from a regional-scale ductile shear zone in the Coastal Range of central Chile (32 S). J. S. Am. Earth Sci. 17 (3), 209–226.

Aron, F., Allmendinger, R.W., Cembrano, J., González, G., Yáñez, G., 2013. Permanent fore-arc extension and seismic segmentation: insights from the 2010 Maule earthquake, Chile. J. Geophys. Res. Solid Earth 118 (2), 724–739.

Arriagada, C., Arancibia, G., Cembrano, J., Martínez, F., Carrizo, D., Van Sint Jan, M., Sáez, E., González, G., Rebolledo, S., Sepúlveda, S.A., Contreras-Reyes, E., 2011. Nature and tectonic significance of co-seismic structures associated with the Mw 8.8 Maule earthquake, central-southern Chile forearc. J. Struct. Geol. 33 (5), 891–897.

Beck, S., Barrientos, S., Kausel, E., Reyes, M., 1998. Source characteristics of historic earthquakes along the central Chile subduction Askew et Alzone. J. S. Am. Earth Sci. 11 (2), 115–129.

Berg, K., Charrier, R., 1987. The Rio Choapa transect; a magmatic profile across the Chilean Andes at 31°30'-32° latitude S. In: Proceedings, Congreso Geológico Argentino, 10th, Tucumán, Argentina. vol. 4, pp. 11–14.

Cembrano, J., González, G., Arancibia, G., Ahumada, I., Olivares, V., Herrera, V., 2005. Fault zone development and strain partitioning in an extensional strike-slip duplex: a case study from the Mesozoic Atacama fault system. Tectonophysics 400, 105–125.

Creixell, C., Parada, M.Á., Roperch, P., Morata, D., Arriagada, C., De Arce, C.P., 2006. Syntectonic emplacement of the Middle Jurassic Concón Mafic Dike Swarm, Coastal Range, central Chile (33 S). Tectonophysics 425 (1), 101–122.

Creixell, C., Parada, M.Á., Morata, D., Roperch, P., Arriagada, C., 2009. The genetic relationship between mafic dike swarms and plutonic reservoirs in the Mesozoic of central Chile (30°– 33°45' S): insights from AMS and geochemistry. Int. J. Earth Sci. 98 (1), 177–201.

Creixell, C., Parada, M., Morata, D., Vásquez, P., Pérez de Arce, C., Arriagada, C., 2011. Middle-Late Jurassic to Early Cretaceous transtension and transpression during arc building in Central Chile: evidence from mafic dike swarms. Andean Geol. 38, 37–63.

Dalziel, I.W.D., 1981. Backarc extension in the southern Andes: a review and critical appraisal. Philos. Trans. R. Soc. Lond. Ser. A 300, 319–335.

Deckart, K., Hervé, F., Fanning, C.M., Ramírez, V., Calderón, M., Godoy, E., 2014. Geocronología U-Pb e isótopos de Hf-O en circones del batolito de la Costa Pensilvaniana, Chile. Andean Geol. 41 (1), 49–82.

Domeier, M., Torsvik, T.H., 2014. Plate tectonics in the late Paleozoic. Geosci. Front. 5 (3), 303–350.

Forsythe, R., 1982. The late Palaeozoic to early Mesozoic evolution of southern South America: a plate tectonic interpretation. J. Geol. Soc. 139 (6), 671–682.

Gana, P., Tosdal, R.M., 1996. Geocronología U-Pb y K-Ar en intrusivos del Paleozoico y Mesozoico de la Cordillera de la Costa, Región de Valparaíso, Chile. Andean Geol. 23 (2), 151–164.

Gana, P., Wall, R., Gutiérrez, A., 1996. Mapa Geológico del área de Valparaíso-Curacaví. In: Servicio Nacional de Geología y Minería, Mapas Geológicos, No. 1, escala: 1:100 000, 1 mapa, 1 anexo, Santiago.

Godoy, E., Loske, W., 1988. Tectonismo sinplutónico de dioritas Jurásicas al sur de Valparaíso: datos U-Pb sobre la 'fase Quintay. Andean Geol. 15 (2), 119–127. https://doi.org/10.5027/andgeoV15n2-a02.

Handy, M., Hirth, G., Hovius, N., 2007. Continental fault structure and rheology from the frictional-to-viscous transition downward. In: Tectonic Faults: Agents of Change on a Dynamic Earth, MIT Press, Cambridge, MA, pp. 139–182.

Hervé, F., 1977. Petrology of the crystalline basement of the Nahuelbuta Mountains, south-central Chile. In: Ishikawa, T., Aguirre, L. (Eds.), Comparative Studies on the Geology of the Circumpacific Orogenic Belt in Japan and Chile. Japan Society for the Promotion of Science, Tokyo. 51 p.

Hervé, 1988. Late Paleozoic subduction and accretion in southern Chile. Episodes 11, 183–188.
Hervé, F., Munizaga, F., Parada, M., Brook, M., Pankhurst, R., Snelling, N., Drake, R., 1988. Granitoids of the Coast Range of Central Chile: geochronology and geologic setting. J. S. Am. Earth Sci. 1, 185–194. https://doi.org/10.1016/0895-9811(88)90036-3.
Horton, B.K., 2018. Tectonic regimes of the central and southern Andes: responses to variations in plate coupling during subduction. Tectonics 37, 402–429. https://doi.org/10.1002/2017TC004624.
Kay, S.M., Godoy, E., Kurtz, A., 2005. Episodic arc migration, crustal thickening, subduction erosion, and magmatism in the south-central Andes. Geol. Soc. Am. Bull. 117 (1–2), 67–88.
Kleiman, L.E., Japas, M.S., 2009. The Choiyoi volcanic province at 34 S–36 S (San Rafael, Mendoza, Argentina): implications for the Late Palaeozoic evolution of the southwestern margin of Gondwana. Tectonophysics 473 (3), 283–299.
Lee, J.Y., Marti, K., Severinghaus, J.P., Kawamura, K., Yoo, H.S., Lee, J.B., Kim, J.S., 2006. A redetermination of the isotopic abundances of atmospheric Ar. Geochim. Cosmochim. Acta 70 (17), 4507–4512.
Ludwig, K.R., 2003. User's Manual for Isoplot 3.00, a Geochronlogical Toolkit for Microsoft Excel. vol. 4. Berkeley Geochronology Center, pp.25–32. Special Publication.
Maloney, K.T., Clarke, G.L., Klepeis, K.A., Quevedo, L., 2013. The Late Jurassic to present evolution of the Andean margin: drivers and the geological record. Tectonics 32 (5), 1049–1065.
McDougall, I., Harrison, T.M., 1999. Geochronology and Thermochronology by the $^{40}Ar/^{39}Ar$ Method. Oxford University Press.
Miyashiro, A., 1961. Evolution of metamorphic belts. J. Petrol. 2, 277–311.
Morata, D., Aguirre, L., 2003. Extensional Lower Cretaceous volcanism in the Coastal Range (29°20' – 30°S), Chile: geochemistry and petrogenesis. J. S. Am. Earth Sci. 16, 459–476.
Morata, D., Higgins, M., Varas, M.I., 2009. Rhythmic gabbroic layering in the Illapel Plutonic Complex (Coastal Cordillera of central Chile): Petrography and field relationships. In: Proceedings, Congreso Geológico Chileno, 12th, Santiago, Chile. vol. 22, pp. 26.
Mpodozis, C., Ramos, V.A., 1989. The Andes of Chile and Argentina. In: Ericksen, G.E., Calqas Pinochet, M.T., Reinemud, J.A. (Eds.), Geology of the Andes and Its Relation to Hydrocarbon and Mineral Resources. Earth Sciences Series, Houston, vol. 11. Circumpacific Council for Energy and Mineral Resources, pp. 59–90.
Mpodozis, C., Ramos, V.A., 2008. Tectónica Jurásica en Argentina y Chile: Extensión, Subducción Oblicua, Rifting, Deriva y Colisiones? Rev. Asoc. Geol. Argent. 63 (4), 481–497.
Parada, M.A., Nyström, J.O., Levi, B., 1999. Multiple sources for the Coastal Batholith of central Chile (31–34 S): geochemical and Sr–Nd isotopic evidence and tectonic implications. Lithos 46 (3), 505–521.
Parada, M.A., Féraud, G., Fuentes, F., Aguirre, L., Morata, D., Larrondo, P., 2005. Ages and cooling history of the Early Cretaceous Caleu pluton: testimony of a switch from a rifted to a compressional continental margin in central Chile. J. Geol. Soc. 162 (2), 273–287.
Passchier, C.W., Trouw, R.A.J., 2005. Microtectonics, second ed. Springer-Verlag, Berlin.
Ramos, V.A., Folguera, A., 2005. Tectonic evolution of the Andes of Neuquén: Constraints derived from the magmatic arc and foreland deformation. In: Veiga, G.D., Spalletti, L.A., Howell, J.A., Schwarz, E. (Eds.), The Neuquén Basin, Argentina: A Case Study in Sequence Stratigraphy and Basin Dynamics. vol. 252. Geological Society, London, pp. 15–35. Special Publications.
Renne, P.R., Swisher, C.C., Deino, A.L., Karner, D.B., Owens, T.L., DePaolo, D.J., 1998. Intercalibration of standards, absolute ages and uncertainties in 40Ar/39Ar dating. Chem. Geol. 145 (1–2), 117–152.
Richter, P.P., Ring, U., Willner, A.P., Leiss, B., 2007. Structural contacts in subduction complexes and their tectonic significance: the Late Palaeozoic coastal accretionary wedge of central Chile. J. Geol. Soc. 164 (1), 203–214.
Rivera, O., Cembrano, J., 2000. Modelo de formación de cuencas volcano-tectónicas en zonas de transferencia oblicuas a la cadena andina: el caso de las cuencas oligo-miocénicas de Chile central y su relación con estructuras NWW-NW (33°00–34°30S). In: Proceedings 9th Congreso Geológico Chileno, Puerto Varas. vol. 2, pp. 631–636.

Sabaj, R., 2008. Identicación y caracterización de estructuras potencialmente activas en la cordillera de la costa entre los 33° y 33°45'S. In: Memoria de Título, Departamento de Geología. Universidad de Chile, Santiago. 91 p.

Seton, M., Müller, R.D., Zahirovic, S., Gaina, C., Torsvik, T., Shephard, G., Talsma, A., Gurnis, M., Turner, M., Maus, S., Chandler, M., 2012. Global continental and ocean basin reconstructions since 200 Ma. Earth Sci. Rev. 113 (3), 212–270.

Siña, A., 1987a. Geología y petrogénesis de las rocas plutónicas del batolito de la costa entre Algarrobo y Rocas de Santo Domingo (Chile central 33° 31'S), Región de Valparaíso. (Unpublished thesis), 139 p Universidad de Chile, Santiago.

Siña, A., 1987b. El Batolito de la Costa entre Algarrobo y Rocas de Santo Domingo (Chile central, 33°30'S): geología e interpretaciones petrogenéticas. Comunicaciones 38, 47–66.

Siña, A., Parada, M., 1985. Los granitoides de rocas de Santo Domingo: antecedentes de terreno, petrográficos y de química de elementos mayores para una mezcla de magmas. In: Proceedings, Congreso Geológico Chileno, 4th, Antofagasta, Chile. vol. 3. pp. 512–530.

Vásquez, P., Glodny, J., Franz, G., Frei, D., Romer, R.L., 2011. Early Mesozoic Plutonism of the Cordillera de la Costa (34–37 S), Chile: constraints on the onset of the Andean Orogeny. J. Geol. 119 (2), 159–184.

Vernon, R.H., 2004. A Practical Guide to Rock Microstructure. Cambridge University Press.

Wall, R., Gana, P., Gutiérrez, A., 1996. Geología de la Hoja Santiago, área de San Antonio-Melipilla, regiones de Valparaíso, Metropolitana y del Libertador General Bernardo O'Higgins. In: Servicio Nacional de Geología y Minería, Chile, Mapas Geológicos 2, escala 1:100 000.

Webber, J.R., Klepeis, K.A., Webb, L.E., Cembrano, J., Morata, D., Mora-Klepeis, G., Arancibia, G., 2015. Deformation and magma transport in a crystallizing plutonic complex, Coastal Batholith, central Chile. Geosphere 11 (5), 1–26. https://doi.org/10.1130/GES01107.1.

Willner, A.P., 2005. Pressure–temperature evolution of a Late Palaeozoic paired metamorphic belt in North–Central Chile (34–35 30′ S). J. Petrol. 46 (9), 1805–1833.

Willner, A.P., Thomson, S.N., Kröner, A., Wartho, J.A., Wijbrans, J.R., Hervé, F., 2005. Time markers for the evolution and exhumation history of a late palaeozoic paired metamorphic belt in north–central Chile (34–35 30' S). J. Petrol. 46 (9), 1835–1858.

Willner, A.P., Richter, P.P., Ring, W., 2009. Structural overprint of a late Paleozoic accretionary system in north-central Chile (34°-35°S) during post-accretional deformation. Andean Geol. 36 (1), 17–36.

Willner, A.P., Massonne, H.J., Ring, U., Sudo, M., Thomson, S.N., 2012. P–T evolution and timing of a late Palaeozoic fore-arc system and its heterogeneous Mesozoic overprint in north-central Chile (latitudes 31–32 S). Geol. Mag. 149 (02), 177–207.